Frequency-dependent squeezing for gravitational-wave detection through quantum teleportation

Yohei Nishino,[1,2,*] Stefan Danilishin,[3,4] Yutaro Enomoto,[5] and Teng Zhang[6]

[1]*Department of Astronomy, University of Tokyo, Bunkyo, Tokyo 113-0033, Japan*

[2]*Gravitational Wave Science Project, National Astronomical Observatory of Japan, Mitaka City, Tokyo 181-8588, Japan*

[3]*Department of Gravitational Waves and Fundamental Physics, Maastricht University, 6200 MD Maastricht, The Netherlands*

[4]*Nikhef - National Institute for Subatomic Physics, Science Park 105, 1098 XG Amsterdam, The Netherlands*

[5]*Department of Applied Physics, The University of Tokyo, Bunkyo, Tokyo 113-0033, Japan*

[6]*School of Physics and Astronomy and Institute of Gravitational Wave Astronomy, University of Birmingham, Edgbaston, Birmingham B15 2TT, United Kingdom*

(Received 25 March 2024; revised 4 July 2024; accepted 8 July 2024; published 1 August 2024)

Ground-based interferometric gravitational-wave detectors are highly precise sensors for weak forces, limited in sensitivity across their detection band by quantum fluctuations of light. Current and future instruments address this limitation by injecting frequency-dependent squeezed vacuum into the detection port, utilizing narrow-band, low-loss optical filter cavities for optimal rotation of the squeezing ellipse at each signal frequency. This study introduces a scheme of such vacuum injection employing the principles of quantum teleportation which works the same as an arbitrary number of filter cavities without additional kilometer-scale infrastructure. We applied this scheme to a detuned signal-recycled Fabry-Pérot–Michelson interferometer, which is the baseline design of the low-frequency detector within the Einstein Telescope xylophone detector. It is shown that our scheme achieves broadband suppression of quantum noise without requiring additional filter cavities or modifications to the core optics of the main interferometer.

DOI: 10.1103/PhysRevA.110.022601

I. INTRODUCTION

In 2015, the Laser Interferometer Gravitational-Wave Observatory (LIGO) [1] achieved a milestone by detecting the first gravitational wave from a binary-black-hole merger [2]. This heralded the beginning of gravitational-wave astronomy, following which the LIGO-Virgo-KAGRA [3,4] collaboration has identified more than 90 gravitational-wave events [5–8]. Furthermore, the third-generation detectors, i.e., the Cosmic Explorer [9] and the Einstein Telescope [10], striving for tenfold greater sensitivity, will empower the exploration of gravitational-wave signals from the events spanning the entire history of the universe [11,12]. This endeavor will illuminate unresolved inquiries in fundamental physics and cosmology [13–15].

Gravitational-wave detectors serving as highly precise displacement-measurement instruments are limited by quantum noise across most of their frequency band. At low frequencies, the optimal sensitivity of a conventional detector faces the constraints of the standard quantum limit (SQL) [16] as a natural consequence of Heisenberg's uncertainty principle [17]. To overcome the SQL, scientists have proposed a variety of technologies based on the quantum nondemolition measurement principle [18,19]. The mainstream approach for quantum noise reduction in existing and future detectors is frequency-dependent squeezing (FDS) injection [20,21]. The injected squeezed vacuum is produced by means of degenerate parametric down-conversion in nonlinear optical crystals. The squeezing angle at each frequency is optimized by passive optical cavities to cancel out the rotation of the squeezing ellipse due to the ponderomotive effect within the interferometer. Current gravitational-wave detectors employ a single filter cavity for their tuned-broadband configurations [22], as it is sufficient for broadband compensation of the ponderomotive squeezing angle in the narrow-band approximation [23,24]. However, when this approximation breaks down, a larger number of filter cavities become necessary (see Refs. [25,26], for example). In either case, as the scale of the detectors increases, these filter cavities, which are currently at the 100-m scale [27,28], will need to reach the kilometer scale.

The installation of kilometer-scale filter cavities entails substantial costs and technological difficulties. To tackle this challenge, several approaches have been proposed to achieve the required sensitivity without the need for filter cavities. These include the use of electromagnetically induced transparency [29], entangled light and negative-mass atomic spin ensembles [30,31], and small-scale optomechanical filters [32]. Einstein-Podolsky-Rosen (EPR) or *conditional* squeezing was proposed by Ma, *et al.* [33] and experimentally demonstrated in [34–37]. In this scheme, by applying the concept of EPR steering [38,39] to gravitational-wave detectors, the main Fabry-Pérot–Michelson interferometer can be repurposed as a single filter cavity [see Fig. 1(a)].

In this paper, we propose a generalized scheme of the EPR squeezing, employing the concept of quantum teleportation. Quantum teleportation of an optical state is a well-established technique in the field of continuous-variable quantum information processing that was first demonstrated by Furusawa *et al.* based on the Braustein-Kimble scheme [40,41]. Through

*Contact author: yohei.nishino@grad.nao.ac.jp

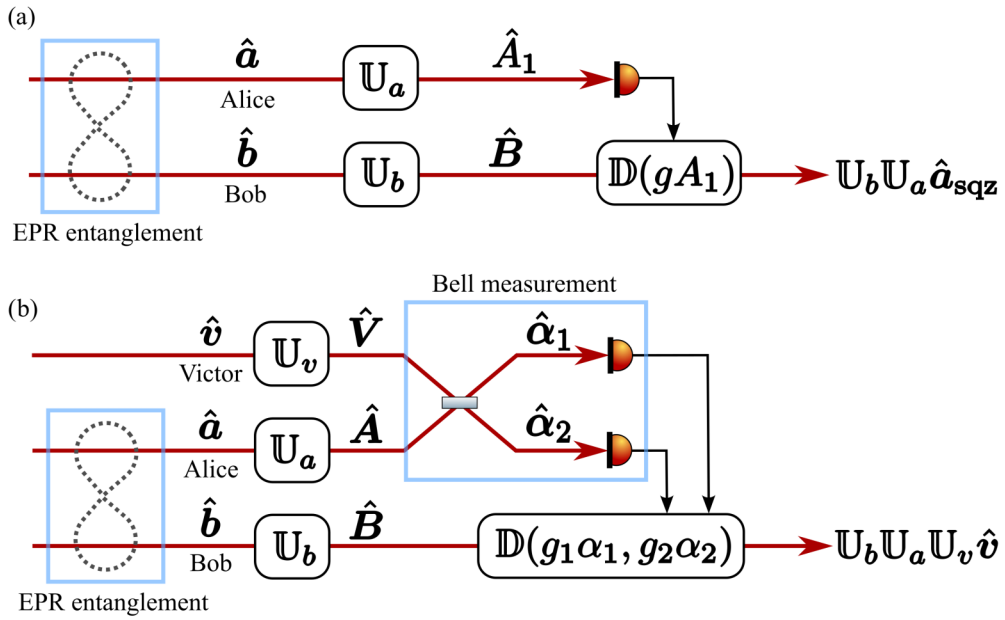

FIG. 1. Schematics of (a) EPR steering and (b) quantum teleportation. We use the two-photon formalism, in which each beam is described by quadrature amplitude operators, where subscripts 1 and 2 denote the amplitude and phase quadratures, respectively. All transformations of the beams are represented by transfer matrices, and $\hat{a}_{\rm sqz}$ is a squeezed vacuum. The Bell observables here are defined as $\hat{\alpha}_1 = (\hat{V}_1 - \hat{A}_1)/\sqrt{2}$ and $\hat{\alpha}_2 = (\hat{V}_2 + \hat{A}_2)/\sqrt{2}$. When Victor's, Alice's, and Bob's states undergo physical transformations, $\mathbb{U}_v$ and $\mathbb{U}_a$, which are assumed to be phase rotations, and $\mathbb{U}_b$, which corresponds to the ponderomotive squeezing, the teleported state is transformed accordingly to $\mathbb{U}_b\mathbb{U}_a\mathbb{U}_v\hat{v}$.

our scheme, one can realize an arbitrary number of operations of quadrature-angle rotation without the use of filter cavities.

The teleportation procedure in the Braustein-Kimble scheme involves Alice, the sending station; Bob, the receiving platform which shares EPR-entangled photons [42]; and Victor, which brings an unknown quantum state and initiates the process [see Fig. 1(b)]. Alice conducts the Bell measurement involving Victor's and her own photons, transmitting the outcome to Bob through the classical communication channel. Bob then displaces his photon based on Alice's information, leading to the successful teleportation of Victor's quantum state. By adding physical operations to Alice's, Bob's, and Victor's paths, described as $\mathbb{U}_{a,b,v}$ in Fig. 1(b), one can also manipulate the final teleported state as $\mathbb{U}_b\mathbb{U}_a\mathbb{U}_v\hat{v}$. Furthermore, Bell measurement extends the limit of participating modes from two to an arbitrary number. By plugging the steered state or the teleported state into the initial state of Victor in a new teleportation protocol, $\hat{v}$, via Bell measurement, one can increase the number of equivalent filter cavities to an arbitrary number (see the detailed discussion in Appendix B).

In the following sections, we illustrate how Quantum Teleportation (QT) squeezing can be implemented in future detectors, which necessitates multiple filter cavities. Specifically, we focus on the low-frequency interferometer of the Einstein Telescope's xylophone detector (ETLF). In the ETLF, the round-trip phase in the signal-extraction cavity is slightly detuned to connect the suspended mirrors by the so-called optical spring [16,43], which enables overcoming the SQL. Additionally, for a narrow-band interferometer such as the ETLF, detuning offers the flexibility to boost the detector's sensitivity [10].

To realize broadband noise suppression for such a detuned configuration, two filter cavities are required: one is for compensating the optical detuning resonance in the interferometer, and the other is for compensating the so-called optical spring resonance from the ponderomotive rigidity effect. We associate the main interferometer response including the ponderomotive squeezing [20] with $\mathbb{U}_b$ in Fig. 1(b) and quadrature rotations by passive cavities with $\mathbb{U}_{v,a}$. Figure 2 shows the implementation. Three beams, Victor, Alice, and Bob, are injected into the interferometer from the antisymmetric port. The interferometer, acting as an empty cavity for Victor and Alice, provides an optimized frequency-dependent quadrature rotation by tuning their center frequencies and the macroscopic lengths of the arm and signal-extraction cavity, which functions as the filter cavities. Bob's frequency is matched to the main laser from the symmetric port; then he sees the interferometer as an active cavity including ponderomotive squeezing [20]. The output is spectrally separated into two detection ports by the output mode cleaners; Bob's beam gets collapsed via homodyne detection, while Victor's and Alice's are detected through Bell measurement. By applying Wiener filters to the two outputs of the Bell measurement, quantum noise suppression is achieved (see Fig. 4 below). In the following sections, we will present the details for each step mentioned above.

II. QUANTUM STATE PREPARATION

The initial quantum states of three beams, Alice, Bob, and Victor, are prepared with a multimode squeezer [44]. The entangled beams, Alice and Bob, are centered at frequencies $\omega_0 + \Delta_a$ and ω_0, created by driving the Optical Parametric Amplifier (OPA) with a pumping beam at frequency $2\omega_0 + \Delta_a$; the squeezed beam, Victor, at frequency $\omega_0 + \Delta_v$, is created by the second pumping beam at frequency $2(\omega_0 + \Delta_v)$

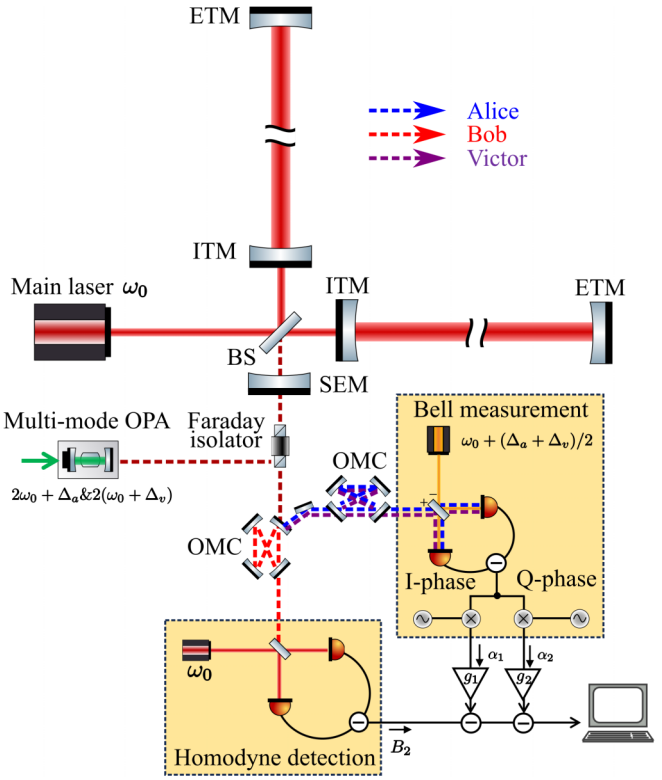

FIG. 2. Configuration of QT squeezing. The OPA in the antisymmetric port is pumped at two frequencies, $2\omega_0+\Delta_a$ and $2(\omega_0+\Delta_v)$, generating entanglement at the sideband frequencies symmetrically [see also Fig. 3(b)]. The former pumping results in a two-mode EPR entanglement, Alice and Bob, while the latter forms a squeezed state, Victor. Three beams are injected through a Faraday isolator. The central part consists of a signal-recycled Fabry-Pérot-Michelson interferometer, which includes the beam splitter (BS), input-test mass (ITM), end-test mass (ETM), and signal-extraction mirror (SEM). The interferometer is pumped at the frequency ω_0, matching Bob's frequency. The output is spectrally separated by an output mode cleaner (OMC). Bob's beam is collapsed at the homodyne detection, while Victor's and Alice's beams are detected through Bell measurement: two beams are combined with local oscillator (LO) fields with the LO angle $\xi_{\rm LO}$ and are subsequently detected by two photodetectors. The outputs are subtracted from each other and demodulated by two demodulation angles. The two sets of measurement data are combined using the optimal filter gain (g_1 g_2), and finally, we achieve quantum noise suppression.

[see Fig. 3(a)]. Here, Δ_a is supposed to be a free spectral range (FSR) of the OPA cavity away from Bob's frequency to retain the resonant conditions of the entangled beam, and $\Delta_a-2\Delta_v$ equals the multiples of the FSR of the OPA cavity (see Fig. 3).

In two-photon formalism [45,46], the zero-mean random fluctuations of the light field are described by a two-dimensional vector consisting of the operators of the amplitude and phase quadrature, and for Alice, Bob, and Victor, $\hat{a}=\{\hat{a}_{1,\Omega},\ \hat{a}_{2,\Omega}\}^{\rm T}$, $\hat{b}=\{\hat{b}_{1,\Omega},\ \hat{b}_{2,\Omega}\}^{\rm T}$, and $\hat{v}=\{\hat{v}_{1,\Omega},\ \hat{v}_{2,\Omega}\}^{\rm T}$, where Ω is the sideband frequency and the superscript T stands for the transpose. Below we omit the superscript Ω for simplicity.

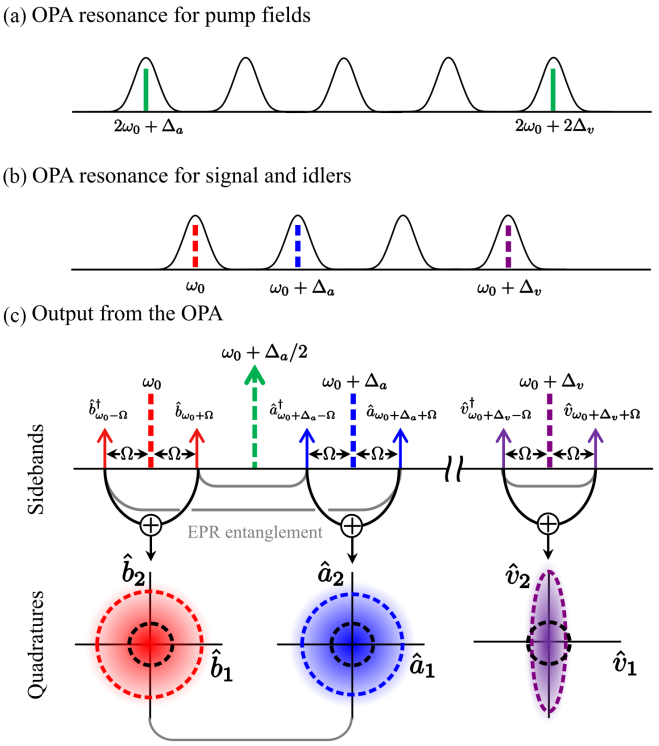

FIG. 3. The OPA resonance for (a) two pump fields and (b) the signal and idlers. In this specific case two pump fields are separated by five FSRs of the OPA cavity, and the frequency difference between Victor and Bob is 3 time larger than that of Alice and Bob. (c) Schematics of three beams. The top and bottom panels show fields in the sideband and quadrature pictures, respectively. The OPA is pumped at two frequencies, $2\omega_0+\Delta_a$ and $2\omega_0+2\Delta_v$, generating entanglement at the sideband frequencies symmetrically. The former pumping results in a two-mode EPR entanglement, Alice and Bob, while the latter forms a squeezed state, Victor.

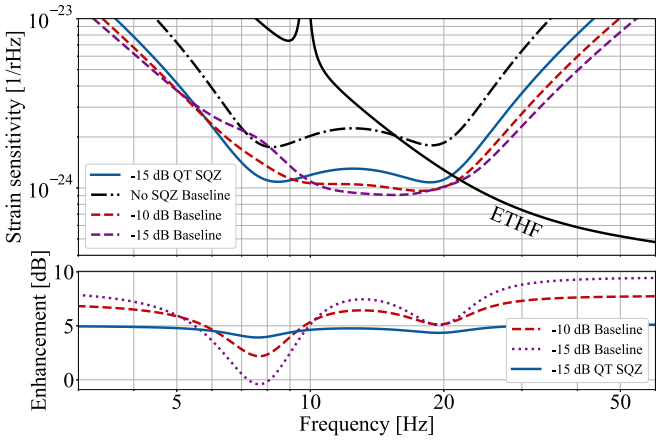

FIG. 4. Top: Quantum-noise-limited strain sensitivity of the ETLF. The red dashed and solid blue curves represent the baseline FDS with −10-dB squeezing and QT squeezing, respectively. The dashed purple curve is the baseline FDS with −15-dB squeezing. We also show the sensitivity of the High-frequency interferometer of the Einstein Telescope's xylophone detector, which covers the frequency region above 20 Hz. Bottom: Quantum noise enhancement in power-spectral density compared to the nonsqueezed case of the baseline FDS (shown by the dash-dotted curve in the top panel).

As shown by Duan *et al.* [47], the strength of the EPR entanglement of Alice's and Bob's states can be expressed in terms of the spectral densities of the four EPR operators, $(\hat{a}_i \pm \hat{b}_i)/\sqrt{2}$, as

$$S_{(\hat{a}_1 \pm \hat{b}_1)/\sqrt{2}} = e^{\pm 2r}, \quad S_{(\hat{a}_2 \pm \hat{b}_2)/\sqrt{2}} = e^{\mp 2r}, \tag{1}$$

where r signifies the squeezing factor. When $r \to \infty$, the noise spectra of $S_{(\hat{a}_1 - \hat{b}_1)/\sqrt{2}}$ and $S_{(\hat{a}_2 + \hat{b}_2)/\sqrt{2}}$ approach zero, corresponding to the original EPR entanglement [42]. In a more general situation, with the quadrature $\hat{a}_{-\theta} = \hat{a}_1 \cos\theta - \hat{a}_2 \sin\theta$ measured, the quadrature $\hat{b}_\theta = \hat{b}_1 \cos\theta + \hat{b}_2 \sin\theta$ is conditionally squeezed and vice versa. The spectral density of the conditional squeezed field reads

$$S^{\hat{a}_{-\theta}}_{\hat{b}_\theta \hat{b}_\theta} = 1/\cosh(2r), \quad S^{\hat{a}_{-\theta}}_{\hat{b}_{\pi/2+\theta} \hat{b}_{\pi/2+\theta}} = \cosh(2r). \tag{2}$$

Victor's amplitude (phase) quadrature experiences (anti)squeezing as

$$S_{\hat{v}_1 \hat{v}_1} = e^{-2r}, \quad S_{\hat{v}_2 \hat{v}_2} = e^{2r}. \tag{3}$$

Throughout this work, we assume uniform squeeze factors for each pumping frequency for the sake of simplicity.

III. NOISE SUPPRESSION THROUGH QUANTUM TELEPORTATION

After passing through the main interferometer, Bob's readout phase quadrature, represented by the observable B_2, can be written as

$$\hat{B}_2 = \Gamma e^{i\beta_b} (\hat{b}_1 \cos\theta_b - \hat{b}_2 \sin\theta_b), \tag{4}$$

where Γ, θ_b, and β_b represent the frequency-dependent gain, quadrature rotation, and phase shift from the ponderomotive squeezing as defined in [48] (see also Appendix A). In order to squeeze $\hat{B}_2$, we need to displace its photon at the input stage by applying quadrature rotation $-\theta_b$. This can be prepared by applying a phase rotation to its entangled pair, Alice, θ_a, and displacing Victor's state with quadrature rotation, θ_v, where $\theta_a + \theta_v = -\theta_b$ is required. By configuring detunings of Alice and Victor with respect to the main interferometer, the interferometer can function as an empty optical cavity for Victor and Alice and can provide desired quadrature rotations at its output.

A. Bell measurement

The teleportation of Victor's state to Bob requires a Bell measurement between Alice and Victor. In the Bell measurement, a local oscillator at frequency $\omega_0 + (\Delta_a + \Delta_v)/2$ is combined with Alice and Victor by a half beam splitter. Subsequently, the two output beams are detected by two photodetectors, and their photon currents are demodulated at frequency $(\Delta_v - \Delta_a)/2$. By setting the local oscillator angle to $-\pi/2$ and properly choosing the demodulation phase, Bell observables can be carried out (details are given in Appendix C):

$$\hat{\alpha} = \begin{pmatrix} \hat{\alpha}_1 \\ \hat{\alpha}_2 \end{pmatrix} = \frac{1}{\sqrt{2}} \begin{pmatrix} \hat{V}_1 - \hat{A}_1 \\ \hat{V}_2 + \hat{A}_2 \end{pmatrix}, \tag{5}$$

where $\hat{A}_1 = e^{i\beta_a}(\hat{a}_1 \cos\theta_a - \hat{a}_2 \sin\theta_a)$ and $\hat{A}_2 = e^{i\beta_a}(\hat{a}_1 \sin\theta_a + \hat{a}_2 \cos\theta_a)$ and $\hat{V}_1 = e^{i\beta_v}(\hat{v}_1 \cos\theta_v - \hat{v}_2 \sin\theta_v)$ and $\hat{V}_2 = e^{i\beta_v}(\hat{v}_1 \sin\theta_v + \hat{v}_2 \cos\theta_v)$ are the quadratures of Alice's and Victor's beams after passing through the interferometer. β_v and β_a are the average phases of both quadratures.

B. Postprocessing

The classical communication channel can be built with displacement operation or, equivalently, achieved through postprocessing by combining $\hat{B}_2$ with $g_1\hat{\alpha}_1$ and $g_2\hat{\alpha}_2$, namely,

$$\hat{B}_2^{\text{tel}} = \hat{B}_2 - g_1\hat{\alpha}_1 - g_2\hat{\alpha}_2, \tag{6}$$

where g_1 and g_2 are filter gains, whose optimal values can be derived by

$$g_1 = \frac{S_{\hat{B}_2\hat{\alpha}_1} S_{\hat{\alpha}_2\hat{\alpha}_2} - S_{\hat{\alpha}_2\hat{\alpha}_1} S_{\hat{B}_2\hat{\alpha}_2}}{S_{\hat{\alpha}_1\hat{\alpha}_1} S_{\hat{\alpha}_2\hat{\alpha}_2} - \left|S_{\hat{\alpha}_1\hat{\alpha}_2}\right|^2}, \tag{7}$$

$$g_2 = \frac{S_{\hat{B}_2\hat{\alpha}_2} S_{\hat{\alpha}_1\hat{\alpha}_1} - S_{\hat{\alpha}_1\hat{\alpha}_2} S_{\hat{B}_2\hat{\alpha}_1}}{S_{\hat{\alpha}_1\hat{\alpha}_1} S_{\hat{\alpha}_2\hat{\alpha}_2} - \left|S_{\hat{\alpha}_1\hat{\alpha}_2}\right|^2} \tag{8}$$

(for more details see Appendix A). In an idealized case without imperfections, we can obtain the eventual noise spectrum density of B_2^{tel},

$$S^{\text{tel}}_{\hat{B}_2\hat{B}_2} = |\Gamma|^2 \frac{1 + e^{-2r}\cosh 2r}{e^{-2r} + \cosh 2r} \xrightarrow{r \gg 1} |\Gamma|^2 \frac{3}{e^{2r}} \tag{9}$$

(see detailed derivations in Appendix A). Taking into account that the gravitational-wave signal sidebands are not affected throughout the postprocessing, Eq. (9) indicates that the strain sensitivity is improved by a factor of $3/e^{2r}$ in power across a wide range of frequencies with sufficient squeezing, which corresponds to the 4.8-dB penalty discussed in Sec. V.

IV. SENSITIVITY COMPARISON

In the top panel of Fig. 4, we show the quantum noise-limited sensitivity of the ETLF [10] with the conventional frequency-dependent squeezing (hereafter called the baseline FDS) and QT squeezing. As a comparison we also plot the enhancement factor compared to nonsqueezed case of the baseline FDS (denoted as "No SQZ Baseline"). As shown, the detuned configuration creates a dip of optical spring at very low frequency (<10 Hz), enabling us to broaden the detector's total bandwidth to lower frequency than a tuned configuration. The parameters considered, including imperfections such as losses and phase noises, are consistent with the current design of the ETLF employing filter cavities, except for the squeezing level, as shown in Table I. Detuning frequencies Δ_a and Δ_v are also shown in Table I, while the method for parameter searching and details of macroscopic length tuning are discussed in Appendix D.

In general, QT squeezing exhibits sensitivity levels that are inferior to those of the baseline FDS, as shown in most of the frequency range in the bottom panel of Fig. 4. This disparity arises from the 4.8-dB penalty inherent in QT squeezing, as indicated by Eq. (9), and there are also threefold optical losses stemming from the three optical paths.

TABLE I. Parameters for squeezing in the ETLF.

Parameter	Baseline FDS	QT squeezing
Detuning of the SEC (rad)	0.75	0.75
Filter-cavity length (km)	1	
Arm round trip loss (ppm)	45	45
SEC loss (ppm)	1000	1000
Injection loss (%)	4	4
Readout loss (%)	3	3
Filter cavity round-trip loss (ppm)	20	
Squeezer noise rms (mrad)	10	10
Local oscillator rms (mrad)	10	10
SEC length rms (pm)	1	1
Filter-cavity length rms (pm)	1	
Detuning Δ_a (MHz)		∼319
Detuning Δ_v (MHz)		∼962
Squeezing level (dB)	−10	−15

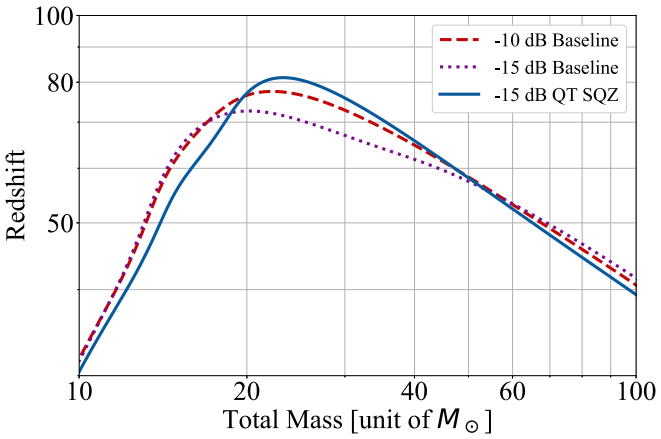

FIG. 5. Detection horizon of the ET with three squeezing schemes in the ETLF, i.e., the baseline FDS with −10- and −15-dB squeezing and QT squeezing with −15-dB squeezing.

However, the performance of QT squeezing can potentially surpass that of baseline FDS around the optical spring resonance. The uneven sensitivity enhancement in the baseline scenarios arises from the dephasing of the squeezed vacuum. As studied in [48,49], the dephasing of the squeezed beam will lead to coupling of the noise fluctuation from the antisqueezed quadrature to the squeezed quadrature. Around the resonance, where the effective mechanical susceptibility of the test mass strengthens due to the optical spring effect, the interferometer creates more significant ponderomotive squeezing of the quantum fields interacting with the mirrors, and the dephasing from the filter cavity becomes large. Therefore, the sensitivity is more susceptible to the dephasing effect, particularly at this frequency band, and the optimal input squeezing level is limited to ∼10 dB (see the dashed and dotted curves in the bottom panel of Fig. 4). Such dephasing can stem from the length fluctuation of optical paths and optical losses in detuned cavities. In the baseline FDS, the filter-cavity length is constrained to 1 km due to infrastructure limitations, which were also employed in [50]. In contrast, QT squeezing leverages the stability and length of the 10-km-long arm cavities as filter cavities. The length fluctuation of the arm cavities is well suppressed by multistage suspension and control systems. In the particular case of ETLF with the parameters in Table I, QT squeezing exhibits better sensitivity than the baseline FDS at 8 Hz, as shown in Fig. 4.

As a filter cavity, the 10-km interferometer has lower effective loss than the 1-km filter cavity, evaluated through the term loss per unit length [49]. We take the 1000-ppm loss from Signal Extraction Cavity (SEC) into account, and it turns out the SEC loss is mitigated by the low transmissivity of the input-test masses (see Appendix E for more details). Those result in less effective loss and dephasing, thus allowing a higher input squeezing level. By accommodating −15-dB squeezing to compensate the 4.8-dB penalty, we can achieve an ∼5-dB sensitivity improvement over the whole frequency band. In this particular case, a higher squeezing level up to −17 dB allows us to improve the sensitivity across the overall frequency range (for details, see Fig. 10 in Appendix E).

As a figure of merit, we plot the detection horizon of equal-mass nonspinning compact binary coalescence in Fig. 5. The detection criterion is set at a signal-to-noise ratio of 8. The overall power spectral densities integrate the classical and quantum noise of the ETLF, as well as the total noise of High-frequency interferometer of the Einstein Telescope's xylophone detector, which covers the sensitivity above 20 Hz, as shown in Fig. 5. The horizon plot indicates that the QT squeezing achieves a performance almost equivalent to the baseline FDS; more precisely, QT squeezing shows a slightly better maximum horizon at the cost of the mass range below $20M_\odot$.

V. DISCUSSION

Our scheme attains frequency-dependent squeezing by replacing the arbitrary number of external filter cavities, which would otherwise require additional kilometer-scale vacuum tunnel and suspension systems, with the main interferometer itself through the application of the quantum teleportation technique. When applying the scheme to ETLF, we revealed that it offers a sensitivity advantage around the optical spring resonance which is the primary objective of detuning. It benefits from the long effective length of the arm cavity acting as the filter cavities and contributes to expanding the bandwidth of the whole detector to lower frequencies.

However, we also need to note two drawbacks of the QT squeezing: (1) the factor of 3 (4.8 dB) higher injected squeezing required to reach the same level of detected squeezing at the readout port as achieved by the baseline FDS and (2) the threefold noise contributions from input and output losses, which limit the sensitivity across the entire frequency band (see Fig. 9 in Appendix E). More generally, if N states participate in the teleportation, the eventual squeezing level is degraded, and noise contributions from both input and output loss increase by a factor of N in power.

In addition, it is essential to highlight the technical flexibility of our scheme. The configuration illustrated in Fig. 2 allows for seamless transitions between detuned and tuned configurations. This transition can be achieved by turning off the pumping laser beam for Victor and adjusting the pumping frequency of the other beam, along with the macroscopic lengths of the arm and signal-extraction cavity, effectively

reverting back to the EPR squeezing in [33]. Furthermore, QT squeezing provides the capability to address variations in the SEC detuning by optimizing the parameters of pumping frequencies and macroscopic length tuning. This means we do not need to replace the input mirror of the filter cavity itself to adjust the filter-cavity bandwidth, which might otherwise be required due to practical factors, such as changes in the main laser power or ice formation on the cryogenic mirrors.

ACKNOWLEDGMENTS

The authors are grateful to S. Hild for stimulating discussions and insight into the potential benefits our scheme might bring to the Einstein Telescope and the ANU CGA squeezer group for fruitful discussions about experimental realization. Research by Y.N. is supported by JSPS Grant-in-Aid for JSPS Fellows Grant No. 23KJ0787. T.Z. acknowledges the support of the Institute for Gravitational Wave Astronomy at the University of Birmingham. S.D. is grateful for support from the Faculty of Science and Engineering of Maastricht University and from the European Research Council (within the framework of ERC-2020-AdG Agreement No. 101019978).

APPENDIX A: DERIVATION OF WIENER FILTERS

In the ideal lossless case, the response of a differential mode cavity of the detuned interferometer for the carrier field can be written as follows according to the scaling-law theorem [51]:

$$\begin{pmatrix}\hat{B}_1\\ \hat{B}_2\end{pmatrix} = \frac{1}{\tilde{M}}\begin{pmatrix}C_{11} & C_{12}\\ C_{21} & C_{22}\end{pmatrix}\begin{pmatrix}\hat{b}_1\\ \hat{b}_2\end{pmatrix}, \tag{A1}$$

where

$$\begin{aligned}\tilde{M} &= \{(\gamma - i\Omega)^2 + \delta^2\}\Omega^2 - \delta\Theta,\\ C_{11} &= C_{22} = \Omega^2(\Omega^2 - \delta^2 + \gamma^2) + \delta\Theta,\\ C_{12} &= 2\delta\gamma\Omega^2 - 2\gamma\Theta, C_{21} = -2\delta\gamma\Omega^2.\end{aligned}$$

Here, δ and γ are the effective detuning and half bandwidth. $\Theta = \frac{8\omega_0 P_c}{McL}$ is the normalized optical power, with P_c being the arm circulating power, M being the reduced mass, and L being the arm length. From these relations, Γ, θ_b and β_b in Eq. (4) in the main text can be derived as

$$\begin{aligned}\Gamma &= \frac{\sqrt{C_{21}^2 + C_{22}^2}}{|\tilde{M}|}, \quad \theta_b = -\arctan\left(\frac{C_{22}}{C_{21}}\right),\\ \beta_b &= \arg\tilde{M}^*.\end{aligned} \tag{A2}$$

Combining the measurement data with filter gains (g_1 and g_2) such that $\hat{B}_2^g = \hat{B}_2 - g_1\hat{\alpha}_1 - g_2\hat{\alpha}_2$, we have the noise spectrum

$$\begin{aligned}S_{\hat{B}_2^g\hat{B}_2^g} =& S_{\hat{B}_2\hat{B}_2} + |g_1|^2 S_{\hat{\alpha}_1\hat{\alpha}_1} + |g_2|^2 S_{\hat{\alpha}_2\hat{\alpha}_2}\\ &- g_1^* S_{\hat{B}_2\hat{\alpha}_1} - g_1 S_{\hat{\alpha}_1\hat{B}_2} - g_2^* S_{\hat{B}_2\hat{\alpha}_2} - g_2 S_{\hat{\alpha}_2\hat{B}_2}\\ &+ g_1 g_2^* S_{\hat{\alpha}_1\hat{\alpha}_2} + g_1^* g_2 S_{\hat{\alpha}_2\hat{\alpha}_1},\end{aligned} \tag{A3}$$

where

$$\begin{aligned}S_{\hat{B}_2\hat{B}_2} &= \Gamma^2\cosh 2r,\\ S_{\hat{\alpha}_1\hat{\alpha}_1} &= \frac{e^{-2r}\cos^2\theta_v + e^{2r}\sin^2\theta_v + \cosh 2r}{2},\end{aligned}$$

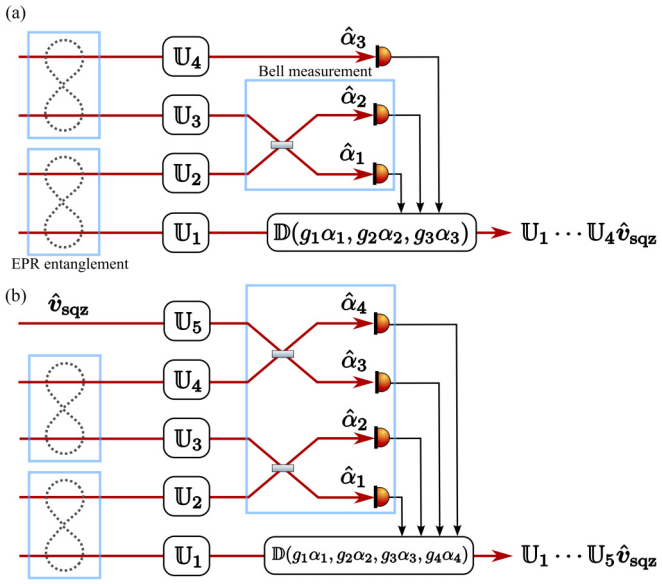

FIG. 6. Schematics of the generalized quantum teleportation squeezing with (a) three equivalent-filter cavities and (b) four filter cavities. Here, $\mathbb{U}_1$ represents the ponderomotive squeezing, other operations represent phase rotations, and $\hat{v}_{\rm sqz}$ is a squeezed vacuum.

$$\begin{aligned}S_{\hat{\alpha}_2\hat{\alpha}_2} &= \frac{e^{-2r}\sin^2\theta_v + e^{2r}\cos^2\theta_v + \cosh 2r}{2},\\ S_{\hat{\alpha}_1\hat{\alpha}_2} &= \frac{(e^{-2r} - e^{2r})\sin\theta_v\cos\theta_v}{2},\\ S_{\hat{B}_2\hat{\alpha}_1} &= S^*_{\hat{\alpha}_1\hat{B}_2} = -\frac{\Gamma e^{i(\beta_b-\beta_a)}\cos\theta_v\sinh 2r}{\sqrt{2}},\\ S_{\hat{B}_2\hat{\alpha}_2} &= S^*_{\hat{\alpha}_2\hat{B}_2} = -\frac{\Gamma e^{i(\beta_b-\beta_a)}\sin\theta_v\sinh 2r}{\sqrt{2}}.\end{aligned}$$

$S_{\hat{B}_2^g\hat{B}_2^g}$ takes its minimum when g_1 and g_2 are Wiener filters determined as follows:

$$\begin{aligned}g_1 &= \frac{S_{\hat{B}_2\hat{\alpha}_1}S_{\hat{\alpha}_2\hat{\alpha}_2} - S_{\hat{\alpha}_2\hat{\alpha}_1}S_{\hat{B}_2\hat{\alpha}_2}}{S_{\hat{\alpha}_1\hat{\alpha}_1}S_{\hat{\alpha}_2\hat{\alpha}_2} - |S_{\hat{\alpha}_1\hat{\alpha}_2}|^2}\\ &= -\frac{\sqrt{2}\Gamma e^{i(\beta_b-\beta_a)}\sinh 2r\cos\theta_v}{\cosh 2r + e^{-2r}},\\ g_2 &= \frac{S_{\hat{B}_2\hat{\alpha}_2}S_{\hat{\alpha}_1\hat{\alpha}_1} - S_{\hat{\alpha}_1\hat{\alpha}_2}S_{\hat{B}_2\hat{\alpha}_1}}{S_{\hat{\alpha}_1\hat{\alpha}_1}S_{\hat{\alpha}_2\hat{\alpha}_2} - |S_{\hat{\alpha}_1\hat{\alpha}_2}|^2}\\ &= -\frac{\sqrt{2}\Gamma e^{i(\beta_b-\beta_a)}\sinh 2r\sin\theta_v}{\cosh 2r + e^{-2r}}.\end{aligned}$$

Note that we used the relation $\theta_b + \theta_a = -\theta_v$. Substituting those into Eq. (A3) leads to the noise spectrum density shown in Eq. (9) in the main text.

APPENDIX B: GENERALIZATION TO *N* PHASE ROTATIONS

Figure 6 illustrates quantum teleportation squeezing to generate an arbitrary number of phase rotations. There are two possible approaches: connecting EPR squeezing and QT squeezing to the QT squeezing protocol, as shown in Figs. 6(a)

and 6(b). The first protocol prepares three phase rotations, while the second prepares four. Inductively, one can achieve an arbitrary number of prefiltering phases by preparing multiple entanglement states and iterating Bell measurements. When one prepares N phase rotations, Wiener filters $\mathbf{g} = (g_1 \quad g_2 \quad \cdots \quad g_N)^\top$ can be expressed as follows:

$$\mathbf{g} = \mathbf{S}_{\alpha\alpha}^{-1}\mathbf{S}_{B\alpha}, \tag{B1}$$

where $\mathbf{S}_\alpha$ and $\mathbf{S}_{B\alpha}$ are the cross-spectral density matrix and vector, respectively, defined as

$$\mathbf{S}_{\alpha\alpha} = \begin{pmatrix} S_{\alpha_1\alpha_1} & S_{\alpha_1\alpha_2} & \cdots & S_{\alpha_1\alpha_N} \\ S_{\alpha_2\alpha_1} & S_{\alpha_2\alpha_2} & \cdots & S_{\alpha_2\alpha_N} \\ \vdots & \vdots & \ddots & \vdots \\ S_{\alpha_N\alpha_1} & S_{\alpha_N\alpha_2} & \cdots & S_{\alpha_N\alpha_N} \end{pmatrix}, \tag{B2}$$

$$\mathbf{S}_{B\alpha} = \begin{pmatrix} S_{B\alpha_1} \\ S_{B\alpha_2} \\ \vdots \\ S_{B\alpha_N} \end{pmatrix}. \tag{B3}$$

APPENDIX C: MATHEMATICAL DESCRIPTION OF BELL MEASUREMENT

We describe the Bell measurement procedure, with specific reference to Sec. II C in [52]. Bell measurement utilizes a coherent laser as the local oscillator (LO) to measure the quadratures $\hat{V}_1 - \hat{A}_1$ and $\hat{V}_2 + \hat{A}_2$ (see Fig. 2 in the main text). The frequency of the LO is precisely tuned to match the central frequency of Victor and Alice. In our specific experimental context, it is necessary to control the LO frequency to $\omega_0 + (\Delta_a + \Delta_v)/2$, a frequency regime in the radio-frequency domain, typically in the megahertz range.

Bell measurement involves several key steps. First, a half beam splitter (HBS) is employed to combine the two idlers with the LO, expressed as

$$E_{r,t}(t) = \frac{S(t) \pm L(t)}{\sqrt{2}}. \tag{C1}$$

Here, $E_{r,t}$ are the reflection and transmission of the HBS. $S(t)$ and $L(t)$ are the output from the interferometer and the LO field, respectively, expressed in the sideband picture as

$$S(t) = \int_{-\Lambda}^{\Lambda} \frac{d\Omega}{2\pi} \{\hat{A}_{\omega_0+\Delta_a+\Omega} e^{-i(\omega_0+\Delta_a+\Omega)t} + \hat{V}_{\omega_0+\Delta_v+\Omega} e^{-i(\omega_0+\Delta_v+\Omega)t} + \text{H.c.}\}, \tag{C2}$$

$$L(t) = De^{i\{\omega_0+(\Delta_a+\Delta_v)/2\}t} + \text{H.c.}, \tag{C3}$$

where $\Lambda \lesssim (\Delta_a + \Delta_v)/2$ is the demodulation bandwidth, D is the complex amplitude, and H.c. represents the Hamiltonian conjugate.

Second, two fields are detected by the photodetectors, combining two outputs to reject classical and quantum fluctuations in the LO field. After the combination, the photocurrent is proportional to the square of the field [Eq. (C1)]:

$$\begin{aligned} i(t) &\propto E_r^2 - E_t^2 \propto S(t)L(t) \\ &= D\int_{-\Lambda}^{\Lambda} \frac{d\Omega}{2\pi} \{A_{\omega_0+\Delta_a+\Omega} e^{i\{(\Delta_v-\Delta_a)-\Omega\}t} \\ &\quad + V_{\omega_0+\Delta_v+\Omega} e^{-i\{(\Delta_v-\Delta_a)+\Omega\}t}\} + \text{H.c.} \\ &\quad + [\text{irrelevant terms at high frequencies}]. \end{aligned} \tag{C4}$$

Finally, by mixing $\cos\{(\Delta_v + \Delta_a)t/2 + \xi_d\}$ and applying a low-pass filter with a cutoff of Λ, one obtains

$$\begin{aligned} O(\xi_d; t) &= D\int_{-\Lambda}^{\Lambda} \frac{d\Omega}{2\pi} \{A_{\omega_0+\Delta_a+\Omega} e^{-i\xi_d} e^{-i\Omega t} + \text{H.c.}\} \\ &\quad + D\int_{-\Lambda}^{\Lambda} \frac{d\Omega}{2\pi} \{V_{\omega_0+\Delta_v+\Omega} e^{i\xi_d} e^{-i\Omega t} + \text{H.c.}\}. \end{aligned} \tag{C5}$$

In the quadrature picture, the quadrature operator A_ζ is defined as

$$A_\zeta = A_1 \sin\zeta + A_2 \cos\zeta, \tag{C6}$$

where

$$A_1 = \frac{A_{\omega_0+\Omega} + A^\dagger_{\omega_0-\Omega}}{\sqrt{2}}, \quad A_1 = \frac{A_{\omega_0+\Omega} - A^\dagger_{\omega_0-\Omega}}{i\sqrt{2}}. \tag{C7}$$

Using those relations, Eq. (C5) leads to

$$O(\xi_d; \Omega) = |D| \int_0^{\Lambda} \frac{d\Omega}{2\pi} e^{-i\Omega t} \{A_{\zeta_A}(\Omega) + V_{\zeta_V}(\Omega)\}, \tag{C8}$$

where $\zeta_A = -\xi_d + \frac{\pi}{2} + \arg D$ and $\zeta_V = \xi_d + \frac{\pi}{2} + \arg D$ (see also Eqs. (9)–(12) in [52]). In the frequency domain, one obtains

$$O(\xi_d; \Omega) = |D| \frac{A_{\zeta_A}(\Omega) + V_{\zeta_V}(\Omega)}{\sqrt{2}}. \tag{C9}$$

The LO angle $\arg D$ is considered a free parameter, determined experimentally, while the demodulation angle ξ_d can be adjusted after detection. By setting $\arg D = \pi/2$, the outputs become $(V_1 - A_1)/\sqrt{2}$ and $(V_2 + A_2)/\sqrt{2}$, with ξ_d of $-\pi/2$ and π, denoted as I and Q phases in Fig. 2 in the main text, respectively.

APPENDIX D: INTERFEROMETER RESPONSE FOR IDLERS

In this section, we examine the response of the central interferometer as a filter cavity for two idlers. We show the parameter optimization process, which is crucial for using the interferometer as a quantum filter cavity per our specific requirements, and then investigate the effect of the arm cavity and SEC losses on those filter parameters in comparison with the conventional filter-cavity scheme.

1. Parameter searching

The coupled cavity formed by the SEC, input-test mass (ITM), and end-test mass functions as a passive optical cavity for two idler beams as (see Fig. 7). Due to the phase shifts acquired in the SEC, the bandwidths for two idlers can be tuned to meet the requirement of filter-cavity bandwidths. To begin, let us examine the bandwidth of the arm cavity, which can be expressed as

$$\gamma_{1\text{arm}} = \frac{cT_{\text{ITM}}}{4L_{\text{arm}}}. \tag{D1}$$

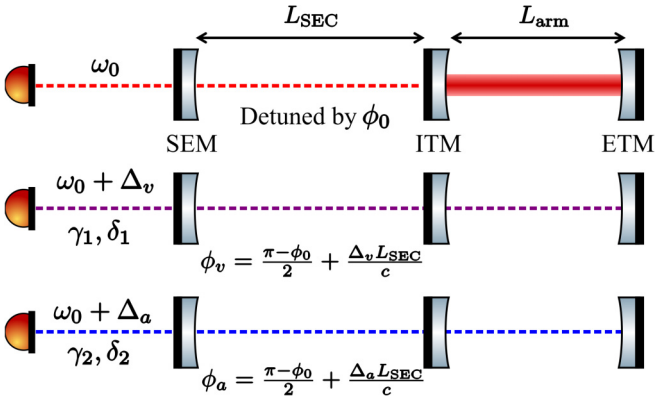

FIG. 7. Resonance conditions for differential mode cavities. Shown from top to bottom are the resonance conditions for Bob, Alice, and Victor.

According to the scaling-law theorem [51,53], the effective bandwidth can be expressed as follows:

$$\gamma = \gamma_{1\mathrm{arm}} \mathrm{Re}\left[\frac{1-\sqrt{R_{\mathrm{SEM}}}e^{2i\phi_{\mathrm{SEC}}}}{1+\sqrt{R_{\mathrm{SEM}}}e^{2i\phi_{\mathrm{SEC}}}}\right] = \frac{\gamma_{1\mathrm{arm}} T_{\mathrm{SEM}}}{1+2\sqrt{R_{\mathrm{SEM}}}\cos 2\phi_{\mathrm{SEC}} + R_{\mathrm{SEM}}}, \tag{D2}$$

leading to the requirement of the round-trip phase ϕ_{SEC}:

$$\phi_{\mathrm{SEC}} = \frac{1}{2}\left[\arccos\left(\frac{T_{\mathrm{SEM}}\frac{\gamma_{1\mathrm{arm}}}{\gamma} - 1 - R_{\mathrm{SEM}}}{2\sqrt{R_{\mathrm{SEM}}}}\right)\right] + n\pi. \tag{D3}$$

Here, n is an integer that determines the number of spectral ranges of the SEC. The phase ϕ_{SEC} for Victor and Alice, denoted as $\phi_{v,a}$, can be described as

$$\phi_{v,a} = \frac{(\omega_0 + \Delta_{v,a})L_{\mathrm{SEC}}}{c} = \frac{\pi - \phi_0}{2} + \frac{\Delta_{v,a} L_{\mathrm{SEC}}}{c}, \tag{D4}$$

where ϕ_0 represents the detuning phase of the SEC for the main carrier. $\phi_{v,a}$ should be tuned to realize the required filter-cavity bandwidth $\gamma_{1,2}$; substituting Eq. (D4) into Eq. (D3), $\Delta_{v,a}$ needs to satisfy the following relation:

$$\Delta_{v,a} = \frac{c}{2L_{\mathrm{SEC}}}\left[\arccos\left(\frac{T_{\mathrm{SEM}}\frac{\gamma_{1\mathrm{arm}}}{\gamma_{1,2}} - 1 - R_{\mathrm{SEM}}}{2\sqrt{R_{\mathrm{SEM}}}}\right) + (2n_{v,a}-1)\pi + \phi_0\right], \tag{D5}$$

where $n_{1,2}$ are free parameters. On the other hand, $\phi_{v,a}$ should also satisfy the following relation to realize the effective detunings $\delta_{1,2}$:

$$\delta_{1,2} = \mathrm{Mod}_{\omega_{\mathrm{FSR}}^{\mathrm{arm}}}(\Delta_{v,a}) - \gamma_{1\mathrm{arm}}\mathrm{Im}\left[\frac{1-\sqrt{R_{\mathrm{SEM}}}e^{2i\phi_{v,a}}}{1+\sqrt{R_{\mathrm{SEM}}}e^{2i\phi_{v,a}}}\right], \tag{D6}$$

where $\omega_{\mathrm{FSR}}^{\mathrm{arm}}$ is the FSR of the arm cavity.

We have four tunable parameters: the macroscopic arm and SEC lengths, $\delta L_{\mathrm{arm}} = q\lambda/2$ and $\delta L_{\mathrm{SEC}} = p\lambda/2$, where q and p are integer values, and $n_{v,a}$, the numbers of SEC spectral ranges contained in $\Delta_{v,a}$. In Table II, we provide the optimal length and frequency tuning parameters. The adjustments required for both the arm and SEC are approximately -2.1 and 4.6 cm, respectively. The detuning frequencies of Victor and Alice are approximately $\Delta_a \sim 319$ MHz and $\Delta_v \sim 962$ MHz, and the corresponding OPA cavity length is ∼94 cm. Figure 8 illustrates a comparison of phase rotations, highlighting the ponderomotive squeezing and the approximate rotations achieved through the combination of the two idlers.

2. Effect of arm-cavity and SEC loss

The arm-cavity loss contains the power loss per each mirror and the transmissivity of the end mirror, which have values of 20 and 5 ppm in the current design of the ET. The arm loss is amplified by the arm cavity approximately by a factor of finesse, which expands the bandwidth of the coupled cavity as a filter cavity for idlers. On the other hand, the SEC-loss contribution to the cavity bandwidth is not significant even though it has a large value of 1000 ppm.

TABLE II. Parameters for the ETLF [10].

Symbol	Definition	Value
λ	Carrier wavelength	1550 nm
T_{arm}	ITM power transmittance	7000 ppm
T_{SEM}	Signal-extraction mirror power transmittance	90%
m	Mirror mass	211 kg
I_0	Power at beam splitter	63 W
ϕ_0	Detuning of the SEC	0.75 rad
$L_{\mathrm{arm}}^{(0)}$	Arm initial length	10 km[a]
$L_{\mathrm{SEC}}^{(0)}$	SEC initial length	100 m
$\gamma_{1\mathrm{arm}}$	Arm-cavity bandwidth	8.35 Hz
γ_1/δ_1	Bandwidth/detuning of the first filter cavity	4.27/19.54 Hz
γ_2/δ_2	Bandwidth/detuning of the second filter cavity	1.64/−7.62 Hz
δL_{arm}	Arm length tuning	30 000λ
δL_{SEC}	SEC length tuning	14 030λ
Δ_a	Detuning of Alice	769 kHz + 213 $\mathrm{FSR}_{\mathrm{SEC}}$[b]
Δ_v	Detuning of Victor	656 kHz + 642 $\mathrm{FSR}_{\mathrm{SEC}}$

[a]To be more precise, $L_{\mathrm{arm}}^{(0)} = 6\,451\,612\,903\lambda$ and $L_{\mathrm{SEC}}^{(0)} = 64\,516\,129\lambda$, where λ is the wavelength of the main laser.
[b]The free spectral range of the SEC (Signal Extraction Cavity) $n_a = 213$, and $n_v = 642$.

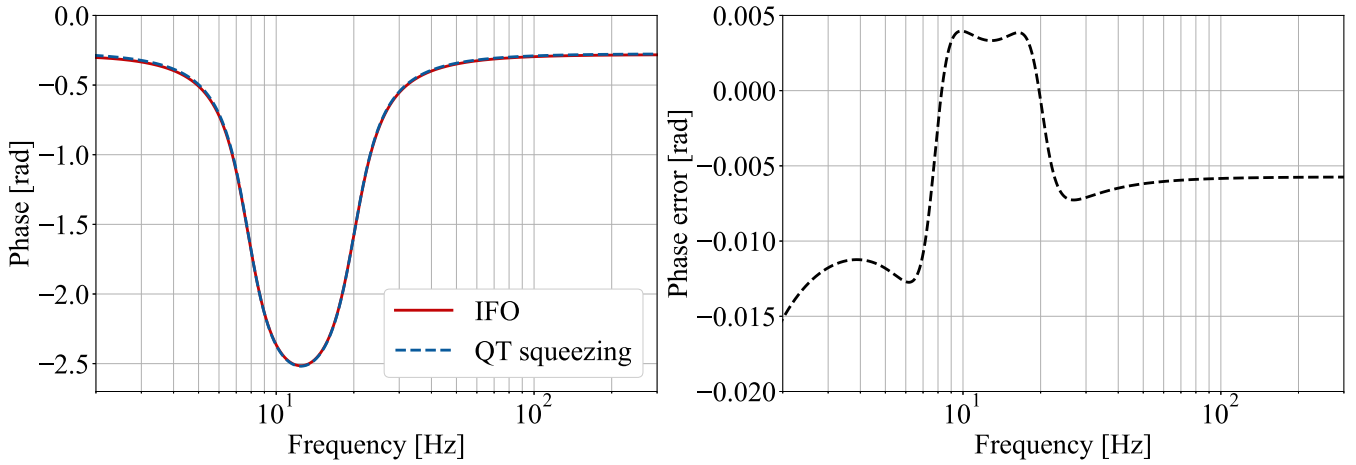

FIG. 8. Left: Quadrature rotations. The solid red curve is caused by the interferometer (IFO), and the dashed blue curve is rotation given to two idlers. Right: Angle error between the two rotations.

According to the scaling-law theorem, the effective bandwidth of the lossy SEC-arm coupled cavity $\gamma_{\rm loss}^{\rm eff}$ can be expressed as follows:

$$\begin{aligned}\gamma_{\rm loss}^{\rm eff} &= \gamma_{\rm loss} + \gamma_2 \\ &= \frac{(T_{\rm SEC} + A_{\rm SEC})\gamma_{\rm 1arm}}{1 + 2\sqrt{R_{\rm SEC}}\cos 2\phi_{\rm SEC} + R_{\rm SEC}} + \frac{cA_{\rm arm}}{4L_{\rm arm}} \\ &= \frac{T_S\gamma_{\rm 1arm}}{1 + 2\sqrt{R_{\rm SEC}}\cos 2\phi_{\rm SEC} + R_{\rm SEC}} + \frac{cA^{\rm eff}}{4L_{\rm arm}}, \end{aligned} \tag{D7}$$

where

$$A^{\rm eff} = \frac{T_{\rm arm}A_{\rm SEC}}{1 + 2\sqrt{R_{\rm SEC}}\cos 2\phi_{\rm SEC} + R_{\rm SEC}} + A_{\rm arm}. \tag{D8}$$

Here, $\gamma_{\rm loss}$ represents the coupled-cavity bandwidth when the arm cavities have no loss, γ_2 is the contribution of the arm-cavity loss to the expansion of the bandwidth, and $\phi_{\rm SEC}$ is the one-way phase inside the SEC for idlers. Equation (D8) is the expansion of the bandwidth due to the losses. Using the current ETLF parameter, the numerator of the first term $T_{\rm arm}A_{\rm SEC}$ is calculated as 7 ppm. Considering the amplification gains of the denominator for two idlers, approximately 1.0 and 2.5, the effective filter-cavity losses are $A_v^{\rm eff} \sim 52$ ppm and $A_a^{\rm eff} \sim 63$ ppm. Since the length of the filter cavity is that of the arm cavity $L_{\rm arm} = 10$ km, the QT squeezing has a smaller noise contribution than conventional filter cavities in terms of the loss per unit length (this is also explained in Refs. [24,49]). Given that the round-trip loss in the filter cavity is $A_{\rm FC} = 20$ ppm and the length $L_{\rm FC} = 1$ km, the discussion above leads to

$$\frac{A_{v,a}^{\rm eff}}{L_{\rm arm}} < \frac{A_{\rm FC}}{L_{\rm FC}},$$

showing that the optical-loss contribution to the expansion of the filter-cavity bandwidth is smaller in the QT squeezing than in the conventional squeezing.

APPENDIX E: NOISE BUDGET

Figure 9 displays the quantum noise budget for the QT squeezing with a squeezing level of −15 dB, alongside the

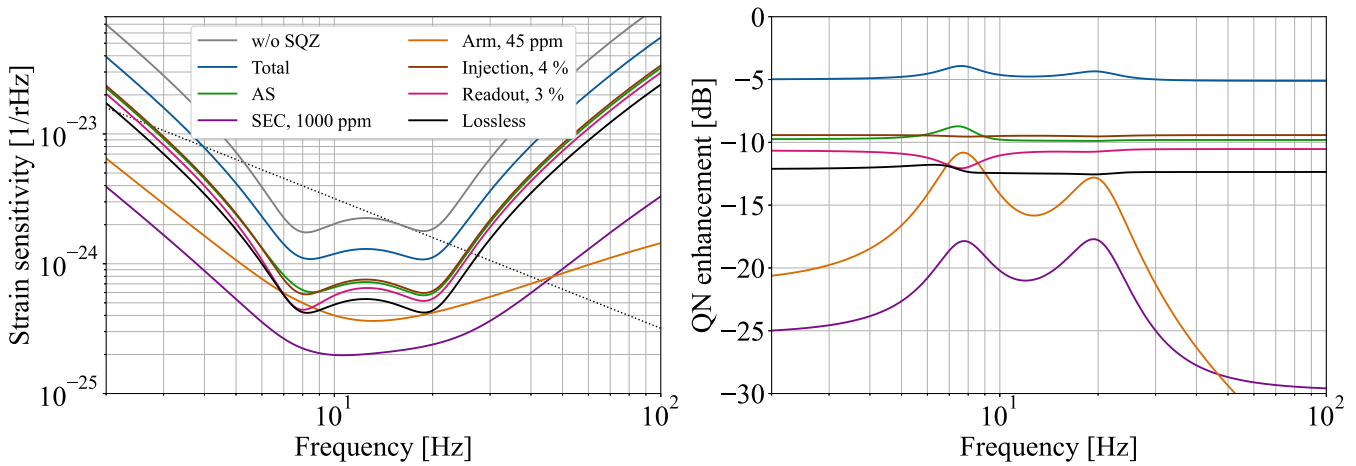

FIG. 9. Left: Noise contributions of each loss source to the strain sensitivity. Phase noises such as squeezer noise rms, local oscillator rms, and SEC length rms are all encompassed within the antisymmetric (AS) noise. The black curve depicts the ideal case without imperfections. Right: Quantum noise enhancement factor (in dB) compared to the noise spectrum without squeezing (shown in gray in the left panel).

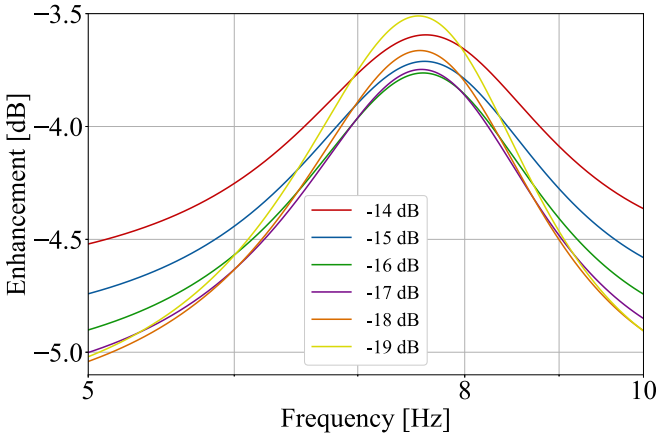

FIG. 10. Quantum noise enhancement with various squeezing levels.

corresponding ETLF results for conventional squeezing. Vacuum fields are introduced into the beam path by each loss source, and their total contribution is obtained by integrating the fields from the same loss point. Four optical losses have been accounted for: (1) a 4% injection loss that considers losses in the OPA cavity and Faraday isolator; (2) a loss of 45 ppm assumed for the round trip of light in the arm, as discussed in Sec. D 2, (3) a loss of 1000 ppm assumed for the signal-extraction mirror, the central beam splitter, and the imperfections of the Michelson interferometer, included in the overall SEC loss; and (4) a 3% loss in readout due to the combined losses in the Faraday isolator, output mode cleaner, and inefficiency of the photodetector. Losses from any source result in uncorrelated vacuum noise in the beam path that reduces the level of squeezing and correlation between EPR-entangled photons.

We evaluate three types of phase noise via root-mean-square (rms) values in our analysis: (1) 10 mrad of squeezer phase noise, which indicates the relative phase noise between the squeezer and the primary laser; (2) 10 mrad of local oscillator rms phase uncertainty, which indicates the relative phase fluctuations between the local oscillator and the primary laser; and (3) 1 pm of SEC rms length variations, which refers to the fluctuations in the optical length of the signal-extraction cavity. These imperfections do not introduce any uncorrelated vacuum noise; rather, they contaminate the output with the contribution from the quadrature of light orthogonal to the one measured, which should not appear in the detection.

As shown in Fig. 9, all noises induced by phase fluctuations are included in the antisymmetric port vacuum. Breaking down the phase noise into parameters called dephasing, as exemplified in [48], to elucidate the specific impact of each phase noise will be the subject of future work. We also plot the noise enhancement curves with various squeezing levels in Fig. 10. Figure 10 shows that the phase noise does not exceed the merit of squeezing when the squeezing level is below −17 dB, while above that the sensitivity deteriorates at the optical spring resonance.

[1] J. Aasi *et al.* (The LIGO Scientific Collaboration), Advanced LIGO, Class. Quantum Grav. **32**, 074001 (2015).

[2] B. P. Abbott *et al.* (LIGO Scientific Collaboration and Virgo Collaboration), Observation of gravitational waves from a binary black hole merger, Phys. Rev. Lett. **116**, 061102 (2016).

[3] F. Acernese *et al.*, Advanced Virgo: A second-generation interferometric gravitational wave detector, Class. Quantum Grav. **32**, 024001 (2015).

[4] (KAGRA Collaboration), KAGRA: 2.5 generation interferometric gravitational wave detector, Nat. Astron. **3**, 35 (2019).

[5] B. P. Abbott *et al.* (LIGO Scientific Collaboration and Virgo Collaboration), GWTC-1: A gravitational-wave transient catalog of compact binary mergers observed by LIGO and Virgo during the first and second observing runs, Phys. Rev. X **9**, 031040 (2019).

[6] R. Abbott *et al.* (LIGO Scientific Collaboration and Virgo Collaboration), GWTC-2: Compact binary coalescences observed by LIGO and Virgo during the first half of the third observing run, Phys. Rev. X **11**, 021053 (2021).

[7] R. Abbott *et al.* (LIGO Scientific Collaboration and Virgo Collaboration), GWTC-3: Compact binary coalescences observed by LIGO and Virgo during the second part of the third observing run, Phys. Rev. X **13**, 041039 (2023).

[8] T. Venumadhav, B. Zackay, J. Roulet, L. Dai, and M. Zaldarriaga, New binary black hole mergers in the second observing run of advanced LIGO and advanced Virgo, Phys. Rev. D **101**, 083030 (2020).

[9] B. P. Abbott *et al.*, Exploring the sensitivity of next generation gravitational wave detectors, Class. Quantum Grav. **34**, 044001 (2017).

[10] S. Hild *et al.*, Sensitivity studies for third-generation gravitational wave observatories, Class. Quantum Grav. **28**, 094013 (2011).

[11] M. Pieroni, A. Ricciardone, and E. Barausse, Detectability and parameter estimation of stellar origin black hole binaries with next generation gravitational wave detectors, Sci. Rep. **12**, 17940 (2022).

[12] M. Maggiore *et al.*, Science case for the Einstein telescope, J. Cosmol. Astropart. Phys. 03 (2020) 050.

[13] B. Sathyaprakash *et al.*, Scientific objectives of Einstein telescope, Class. Quantum Grav. **29**, 124013 (2012).

[14] S. Shankaranarayanan and J. P. Johnson, Modified theories of gravity: Why, how and what? Gen. Relativ. Gravitation **54**, 44 (2022).

[15] B. S. Sathyaprakash, E. Belgacem, D. Bertacca, C. Caprini, G. Cusin, Y. Dirian, X. Fan, D. Figueroa, S. Foffa, E. Hall, J. Harms, M. Maggiore, V. Mandic, A. Matas, T. Regimbau, M. Sakellariadou, N. Tamanini, and E. Thrane, Cosmology and the early universe, arXiv:1903.09260.

[16] V. B. Braginskiĭ, Classical and quantum restrictions on the detection of weak disturbances of a macroscopic oscillator, Sov. JETP **26**, 831 (1968).

[17] C. M. Caves, Quantum-mechanical radiation-pressure fluctuations in an interferometer, Phys. Rev. Lett. **45**, 75 (1980).

[18] K. S. Thorne, R. W. P. Drever, C. M. Caves, M. Zimmermann, and V. D. Sandberg, Quantum nondemolition measurements of harmonic oscillators, Phys. Rev. Lett. **40**, 667 (1978).

[19] V. B. Braginsky and F. Y. Khalili, Quantum nondemolition measurements: The route from toys to tools, Rev. Mod. Phys. **68**, 1 (1996).

[20] H. J. Kimble, Y. Levin, A. B. Matsko, K. S. Thorne, and S. P. Vyatchanin, Conversion of conventional gravitational-wave interferometers into quantum nondemolition interferometers by modifying their input and/or output optics, Phys. Rev. D **65**, 022002 (2001).

[21] C. M. Caves, Quantum-mechanical noise in an interferometer, Phys. Rev. D **23**, 1693 (1981).

[22] J. Mizuno, K. Strain, P. Nelson, J. Chen, R. Schilling, A. Rüdiger, W. Winkler, and K. Danzmann, Resonant sideband extraction: A new configuration for interferometric gravitational wave detectors, Phys. Lett. A **175**, 273 (1993).

[23] P. Purdue and Y. Chen, Practical speed meter designs for quantum nondemolition gravitational-wave interferometers, Phys. Rev. D **66**, 122004 (2002).

[24] F. Y. Khalili, Optimal configurations of filter cavity in future gravitational-wave detectors, Phys. Rev. D **81**, 122002 (2010).

[25] J. Harms, Y. Chen, S. Chelkowski, A. Franzen, H. Vahlbruch, K. Danzmann, and R. Schnabel, Squeezed-input, optical-spring, signal-recycled gravitational-wave detectors, Phys. Rev. D **68**, 042001 (2003).

[26] H. Miao, H. Yang, and D. Martynov, Towards the design of gravitational-wave detectors for probing neutron-star physics, Phys. Rev. D **98**, 044044 (2018).

[27] D. Ganapathy *et al.* (LIGO O4 Detector Collaboration), Broadband quantum enhancement of the LIGO detectors with frequency-dependent squeezing, Phys. Rev. X **13**, 041021 (2023).

[28] F. Acernese *et al.* (Virgo Collaboration), Frequency-dependent squeezed vacuum source for the advanced Virgo gravitational-wave detector, Phys. Rev. Lett. **131**, 041403 (2023).

[29] E. E. Mikhailov, K. Goda, T. Corbitt, and N. Mavalvala, Frequency-dependent squeeze-amplitude attenuation and squeeze-angle rotation by electromagnetically induced transparency for gravitational-wave interferometers, Phys. Rev. A **73**, 053810 (2006).

[30] F. Y. Khalili and E. S. Polzik, Overcoming the standard quantum limit in gravitational wave detectors using spin systems with a negative effective mass, Phys. Rev. Lett. **121**, 031101 (2018).

[31] E. Zeuthen, E. S. Polzik, and F. Y. Khalili, Gravitational wave detection beyond the standard quantum limit using a negative-mass spin system and virtual rigidity, Phys. Rev. D **100**, 062004 (2019).

[32] Y. Ma, S. L. Danilishin, C. Zhao, H. Miao, W. Z. Korth, Y. Chen, R. L. Ward, and D. G. Blair, Narrowing the filter-cavity bandwidth in gravitational-wave detectors via optomechanical interaction, Phys. Rev. Lett. **113**, 151102 (2014).

[33] Y. Ma, H. Miao, B. H. Pang, M. Evans, C. Zhao, J. Harms, R. Schnabel, and Y. Chen, Proposal for gravitational-wave detection beyond the standard quantum limit through EPR entanglement, Nat. Phys. **13**, 776 (2017).

[34] D. D. Brown, H. Miao, C. Collins, C. Mow-Lowry, D. Töyrä, and A. Freise, Broadband sensitivity enhancement of detuned dual-recycled Michelson interferometers with EPR entanglement, Phys. Rev. D **96**, 062003 (2017).

[35] M. J. Yap, P. Altin, T. G. McRae, B. J. J. Slagmolen, R. L. Ward, and D. E. McClelland, Generation and control of frequency-dependent squeezing via Einstein-Podolsky-Rosen entanglement, Nat. Photon. **14**, 223 (2020).

[36] J. Südbeck, S. Steinlechner, M. Korobko, and R. Schnabel, Demonstration of interferometer enhancement through Einstein–Podolsky–Rosen entanglement, Nat. Photon. **14**, 240 (2020).

[37] D. W. Gould, M. J. Yap, V. B. Adya, B. J. J. Slagmolen, R. L. Ward, and D. E. McClelland, Optimal quantum noise cancellation with an entangled witness channel, Phys. Rev. Res. **3**, 043079 (2021).

[38] H. M. Wiseman, S. J. Jones, and A. C. Doherty, Steering, entanglement, nonlocality, and the Einstein-Podolsky-Rosen paradox, Phys. Rev. Lett. **98**, 140402 (2007).

[39] E. G. Cavalcanti, S. J. Jones, H. M. Wiseman, and M. D. Reid, Experimental criteria for steering and the Einstein-Podolsky-Rosen paradox, Phys. Rev. A **80**, 032112 (2009).

[40] A. Furusawa, J. L. Sørensen, S. L. Braunstein, C. A. Fuchs, H. J. Kimble, and E. S. Polzik, Unconditional quantum teleportation, Science **282**, 706 (1998).

[41] S. L. Braunstein and H. J. Kimble, Teleportation of continuous quantum variables, Phys. Rev. Lett. **80**, 869 (1998).

[42] A. Einstein, B. Podolsky, and N. Rosen, Can quantum-mechanical description of physical reality be considered complete? Phys. Rev. **47**, 777 (1935).

[43] A. Buonanno and Y. Chen, Signal recycled laser-interferometer gravitational-wave detectors as optical springs, Phys. Rev. D **65**, 042001 (2002).

[44] T. Zhang, D. Martynov, A. Freise, and H. Miao, Quantum squeezing schemes for heterodyne readout, Phys. Rev. D **101**, 124052 (2020).

[45] B. L. Schumaker and C. M. Caves, New formalism for two-photon quantum optics. II. Mathematical foundation and compact notation, Phys. Rev. A **31**, 3093 (1985).

[46] C. M. Caves and B. L. Schumaker, New formalism for two-photon quantum optics. I. Quadrature phases and squeezed states, Phys. Rev. A **31**, 3068 (1985).

[47] L.-M. Duan, G. Giedke, J. I. Cirac, and P. Zoller, Inseparability criterion for continuous variable systems, Phys. Rev. Lett. **84**, 2722 (2000).

[48] L. McCuller *et al.*, LIGO's quantum response to squeezed states, Phys. Rev. D **104**, 062006 (2021).

[49] P. Kwee, J. Miller, T. Isogai, L. Barsotti, and M. Evans, Decoherence and degradation of squeezed states in quantum filter cavities, Phys. Rev. D **90**, 062006 (2014).

[50] M. Branchesi *et al.*, Science with the Einstein telescope: A comparison of different designs, J. Cosmol. Astropart. Phys. 07 (2023) 068.

[51] A. Buonanno and Y. Chen, Scaling law in signal recycled laser-interferometer gravitational-wave detectors, Phys. Rev. D **67**, 062002 (2003).

[52] A. Buonanno, Y. Chen, and N. Mavalvala, Quantum noise in laser-interferometer gravitational-wave detectors with a heterodyne readout scheme, Phys. Rev. D **67**, 122005 (2003).

[53] S. L. Danilishin and F. Y. Khalili, Quantum measurement theory in gravitational-wave detectors, Living Rev. Relativ. **15**, 5 (2012).